Detection and modeling of Rayleigh wave induced patterns in the ionosphere

Lucie Rolland, Philippe Lognonné, Hiroshi M Munekane

Detection and modeling of Rayleigh wave induced patterns in the ionosphere

Lucie M. Rolland,[1] Philippe Lognonné,[1] and Hiroshi Munekane[2]

Received 27 August 2010; revised 6 February 2011; accepted 4 March 2011; published 21 May 2011.

[1] Global Positioning System (GPS) allows the detection of ionospheric disturbances associated with the vertical displacements of most of the major shallow seismic events. We describe a method to model the time and space distributions of Rayleigh wave induced total electron content (TEC) patterns detected by a dense GPS array. We highlight the conditions for which a part of the ionospheric pattern can be directly measured, at teleseismic distance and above the epicenter. In particular, a satellite elevation angle lower than 40° is a favorable condition to detect Rayleigh wave induced ionospheric waves. The coupling between the solid Earth and its atmosphere is modeled by computing the normal modes of the solid Earth–atmosphere system. We show the dependency of the coupling efficiency on various atmospheric conditions. By summation of the normal modes we model the atmospheric perturbation triggered by a given earthquake. This shows that a part of the observation is a Rayleigh-induced radiation pattern and therefore characteristic of the seismic rupture. Through atmosphere-ionosphere coupling, we model the ionospheric perturbation. After the description of the local geomagnetic field anisotropic effects, we show how the observation geometry is strongly affecting the radiation pattern. This study deals with the related data for two earthquakes with far-field and near-field observations using the Japanese GPS network GEONET: after the 12 May 2008 Wenchuan earthquake (China) and after the 25 September 2003 Tokachi-Oki earthquake (Japan), respectively. Waveforms and patterns are compared with the observed TEC perturbations, providing a new step toward the use of ionospheric data in seismological applications.

Citation: Rolland, L. M., P. Lognonné, and H. Munekane (2011), Detection and modeling of Rayleigh wave induced patterns in the ionosphere, *J. Geophys. Res.*, *116*, A05320, doi:10.1029/2010JA016060.

1. Introduction

[2] The response of the ionosphere to the vibrations of the solid Earth triggered by earthquakes, volcanoes or tsunamis has been extensively studied in the last 20 years. Indeed, a small amount of the released wave energy is transferred to its surrounding atmosphere by dynamic coupling, and vice versa [*Lognonné et al.*, 1998; *Lognonné*, 2009]. At the location of the seismic source or seismic (or tsunami) wavefronts, the vertical displacement of the Earth's surface acts like a piston on the atmosphere. Through continuity of displacement, this displacement generates upward propagating acoustic or gravity waves. The coupling is maximum around the acoustic cutoff frequency (i.e., around 3.7 mHz), where the atmospheric/solid energy ratio is of the order of a few per mill [*Lognonné et al.*, 1998]. The upward propagating vibrations of the atmosphere are exponentially amplified due to the rarefying air density, up to about 200–300 km where attenuation effects (viscosity, thermoconduction, etc.) start to be significant [*Artru et al.*, 2001]. Thereby, a pressure seismic surface wave with a velocity of 1 mm/s on the ground, corresponding to teleseismic surface waves generated by a shallow earthquake with magnitude 8, reaches the maximum of ionization (F2 ionospheric peak) with many tens to a few hundreds of meters per second [*Artru et al.*, 2004].

[3] In the ionosphere the atmospheric neutral waves interact with the plasma through particle collisions, generating electron density fluctuations [*Kherani et al.*, 2009]. These ionospheric perturbations are often detected via radio techniques, such as HF Doppler sounding and Global Positioning System (GPS) ionospheric monitoring. The latter provides an integrated value called total electron content (TEC). This corresponds to the ionospheric electron density integrated along the satellite-receiver line of sight and is expressed in TECU (1 TECU = 10^{16} electrons/m^2).

[4] Two different types of coseismic ionospheric waves perturbations have been recorded so far. The first waves are low-frequency acoustic waves, excited locally by the earthquake rupture. They propagate both vertically and horizontally at sound speed. They were first observed by *Calais and*

[1]Institut de Physique du Globe de Paris, Sorbonne Paris Cité, Université Paris Diderot, UMR 7154 CNRS, Saint-Maur des Fossés, France.
[2]Geospatial Information Authority of Japan, Geography and Crustal Dynamics Research Center, Tsukuba, Japan.

0148-0227/11/2010JA016060

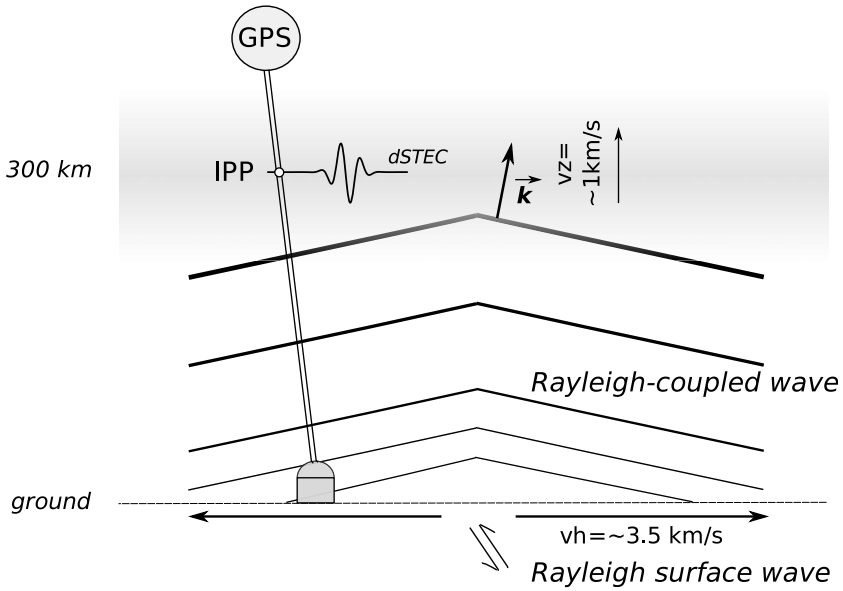

Figure 1. Schematic view of the study. The vertical vibrations of the ground at the passage of Rayleigh waves propagating at 3.5 km/s (v_h) generate an acoustic wave propagating upward at sound speed (v_z), resulting in a plasma perturbation at ionospheric heights. The wave vector **k** is perpendicular to the wavefront and has a zenith angle of about 10° at ionospheric heights.

Minster [1995] with the GPS-TEC technique and successfully modeled through atmospheric ray tracing [*Calais et al.*, 1998; *Heki and Ping*, 2005; *Heki et al.*, 2006; *Afraimovich et al.*, 2010]. Earthquake parameters as energy and fault distribution were also derived.

[5] The second waves are induced by the forcing of the propagating ground or oceanic wavefront. Our paper focuses on Rayleigh wave induced ionospheric signals, and we refer the reader to *Artru et al.* [2005], *Occhipinti et al.* [2006, 2008], *Hickey et al.* [2009, 2010], and *Rolland et al.* [2010] for tsunami wave induced signals. Rayleigh wave induced ionospheric waves have been observed at teleseismic distance (see Figure 1) by three different techniques. The first two are similar and based on HF Doppler [*Artru et al.*, 2004] or over-the-horizon (OTH) radar [*Occhipinti et al.*, 2010] which both monitor the electron vertical oscillations of the ionospheric layer that reflects or refracts the HF signals, typically between 150 and 200 km altitude. The last one is the TEC measurement, which integrates the electron density perturbations between the surface and the satellite [*Dučić et al.*, 2003]. This last technique is sensitive to perturbations occurring at higher altitudes, typically 250 to 350 km. If these three examples have all lead to far-field observations, TEC observations have been also performed in the near field. For example, *Astafyeva et al.* [2009] observe fast propagating Rayleigh wave induced ionospheric waves superimposed to the slow propagating acoustic waves. These two signals can be separated beyond epicentral distance of 700 km, as their propagation speeds are strongly different: about 3 km/s and 600 m/s, respectively.

[6] Let us now address the modeling effects: the vertical velocity of the Rayleigh wave induced ionospheric waves was successfully reproduced by *Artru et al.* [2001], with the summation of Rayleigh fundamental normal modes with atmospheric coupling [*Lognonné et al.*, 1998]. A similar technique was used to compute the near source acoustic signals generated by the eruption of the Montserrat volcano [*Dautermann et al.*, 2009]. The modeling of the TEC signals induced by Rayleigh waves, however, was never published so far and is the main subject of this paper.

[7] Our approach for this modeling is the following. Using the same approach as *Artru et al.* [2004], we compute the atmospheric neutral "winds" (i.e., the neutral atmospheric velocity wavefield) in a 3-D grid surrounding the source area and large enough to include all GPS satellites line of sight. The vertically stratified atmospheric model used is the NRL-MSISE model [*Picone et al.*, 2002], which depends on the local time, location and solar flux. We then model the coupling effects between the neutral and ionized atmosphere accurately, taking into account the a priori ionospheric structure and local magnetic field. We finally compute the electron density perturbation, integrate it along the GPS satellite line of sight and compare it with the TEC measurements. This allows us to model not only single GPS TEC time series, but also to reconstruct 2-D TEC maps sampled by high-density GPS networks in a reasonable computing time.

[8] We apply the process to the Rayleigh wave induced ionospheric disturbances generated by two earthquakes in far-field and near-field conditions, both observed by the Japanese GPS network GEONET. The far-field event is the 12 May 2008 Wenchuan earthquake (M_w 7.9, M_s 8.1) while the near-field event is the 25 September 2003 Tokachi-Oki earthquake (M_w 8.3, M_s 8.1). See Figure 2 for locations.

[9] As the GPS TEC technique is strongly dependent on the observation geometry, we compare the geometries in these two examples for several satellites. Then we define the optimum conditions of observation needed to observe Rayleigh wave induced ionospheric waves. We finally compare

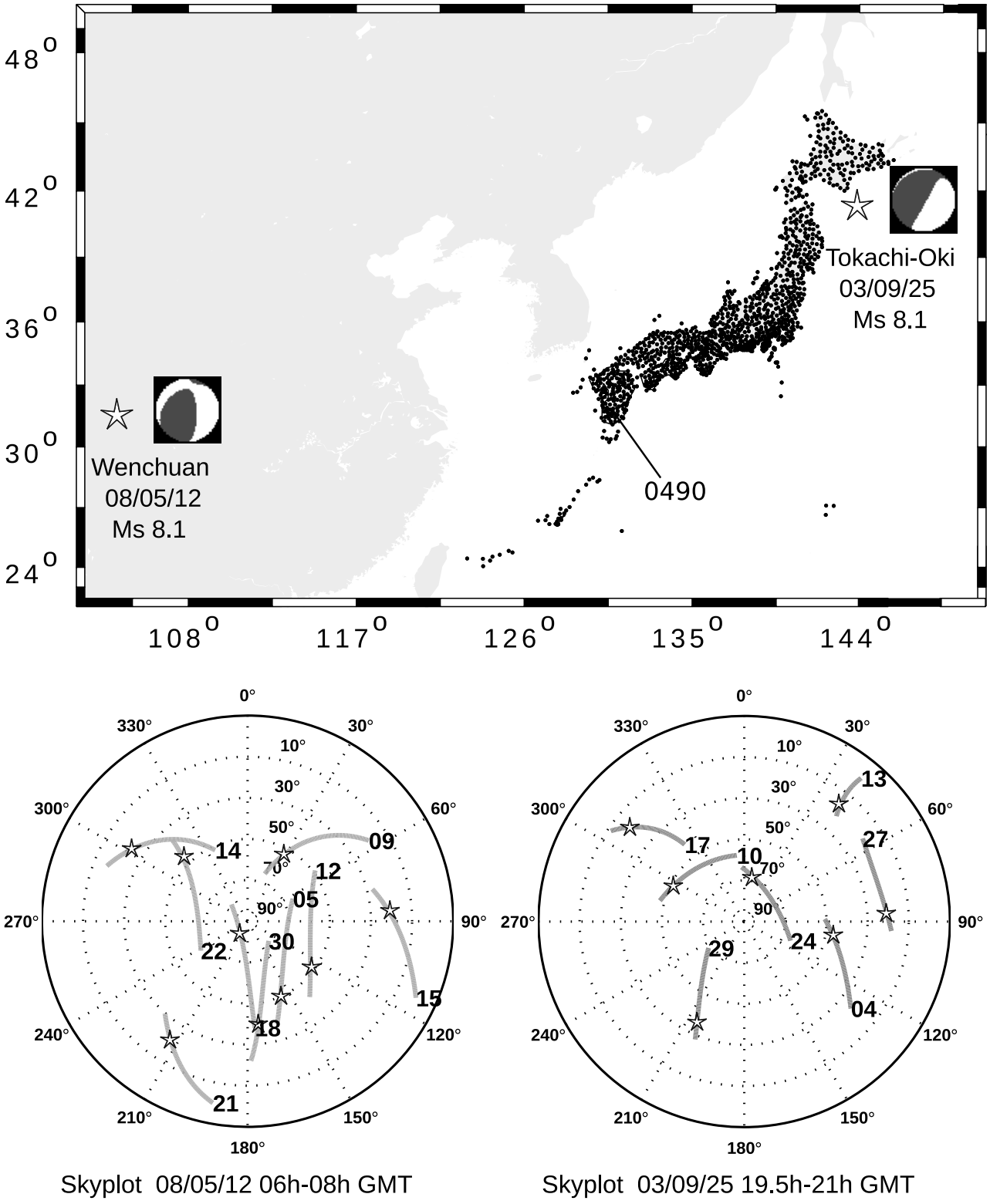

Figure 2. (top) Location of the two seismic events observed with the help of the GEONET dense GPS array, whose receivers are marked by black dots. (bottom) Polar view of the elevation and azimuth angles of the satellites as seen by receiver 0490 (shown on the map) during the unspecified time interval. The stars mark the satellites geometry at seismic origin time. The focal mechanisms diagrams from the Global Centroid-Moment-Tensor database (http://www.globalcmt.org) are also shown.

Table 1. Seismic Source Moment Tensor Solutions Used in Our Simulations and Provided by the Harvard Global Centroid-Moment-Tensor Project[a]

Seismic Event	Origin Time (UT)	Epicenter Location (Lon/Lat, deg)	Depth (km)	Strike/Dip/Slip (deg)	M_o (N m)	dtc (s)	htc (s)
Wenchuan	0628:01	31.44/104.10	12.77	231/35/138	8.97×10^{20}	38.84	21.8
Tokachi-Oki	1950:06	42.21/143.84	28.24	250/11/132	3.05×10^{21}	31.81	33.5

[a]See *Dziewonski and Anderson* [1981]. M_o denotes the scalar moment, dtc is the time shift, and htc is the half duration.

our modeled Rayleigh wave induced GPS TEC disturbances with data and conclude.

2. Background: GPS Ionospheric Mapping Over Japan

[10] For the two events, we use the very dense Japanese GPS Earth Observation Network (GEONET). This network is operated since 1994 by the Geographical Survey Institute (GSI) of Japan and has more than one thousand permanent dual-frequency GPS receivers. Although its primary goal is geodetic monitoring of crustal deformations [*Sagiya*, 2004], it allows high-resolution TEC mapping, with mean distances between the ionospheric piercing points of about 20 km. The 30 s GPS data are freely available from the GEONET public FTP site (http://163.42.5.1) during approximately 1 year after acquisition.

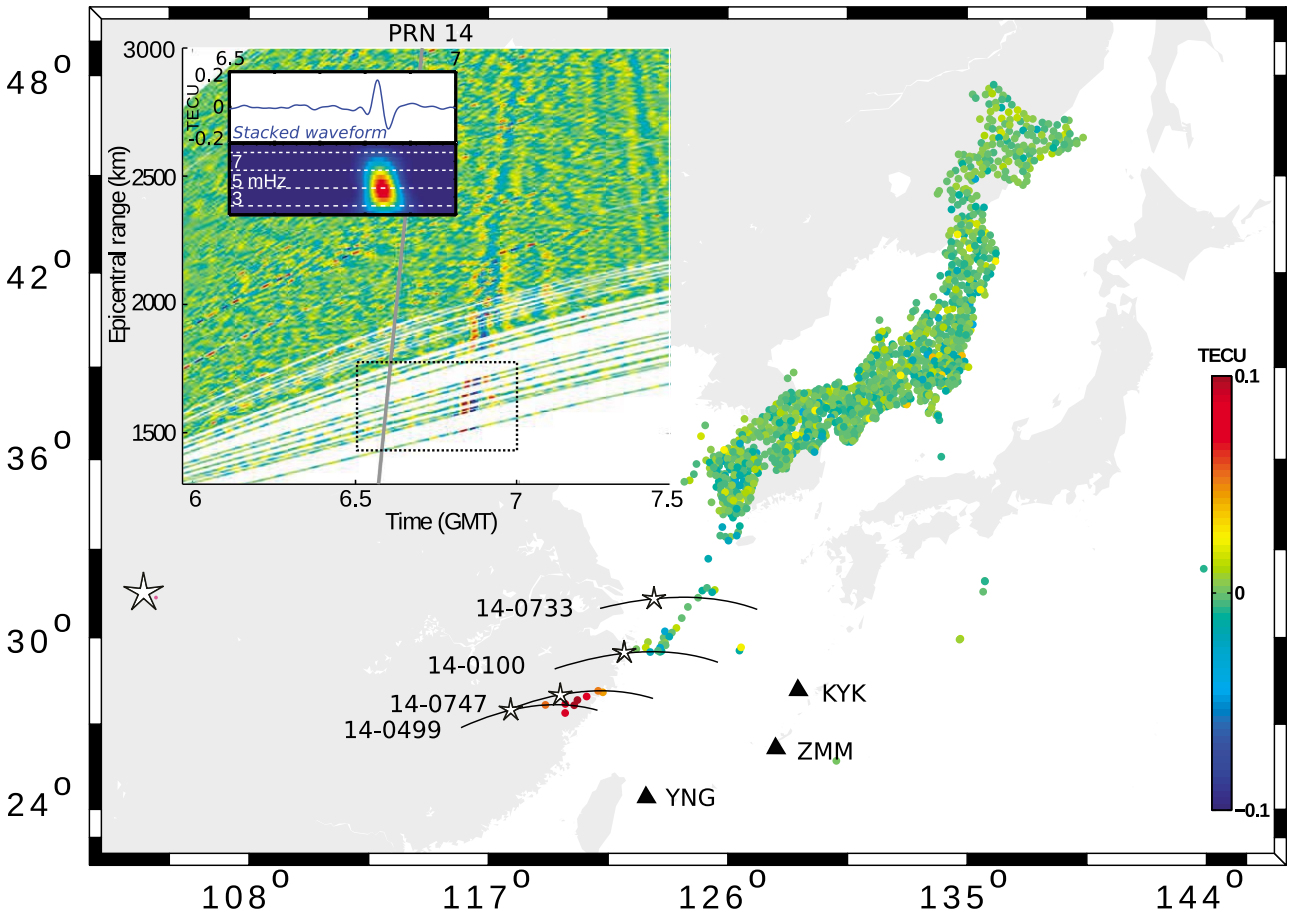

Figure 3. IPP TEC map measured on 12 May 2008 at 0650:00 UT (22 min after the Wenchuan earthquake) using GEONET observing the GPS satellite 14. We also present snapshots from 19 to 29 min after the earthquake in Animation S1 in the auxiliary material. The IPP tracks for the four specified stations are depicted from 0600 to 0730 UT. Nearby seismometers are marked with triangles. The traveltime diagram of the filtered slant TEC at IPPs is shown in the inset. The plain gray line has a 3.5 km/s slope and origin at seismic origin time. It corresponds to the approximate phase velocity on the ground of a Rayleigh surface wave emitted by the earthquake. The dashed gray line indicates the phase velocity of a wave propagating on the ground at sound speed (1 km/s slope). The blue waveform in the inset is a stack of the 8 time series at IPPs located most in the south (in the rectangle). The peak-to-peak time interval is 90 s, and the corresponding spectrogram shows a broad frequency peak centered on 5 mHz. Time series are filtered between 1 and 10 mHz.

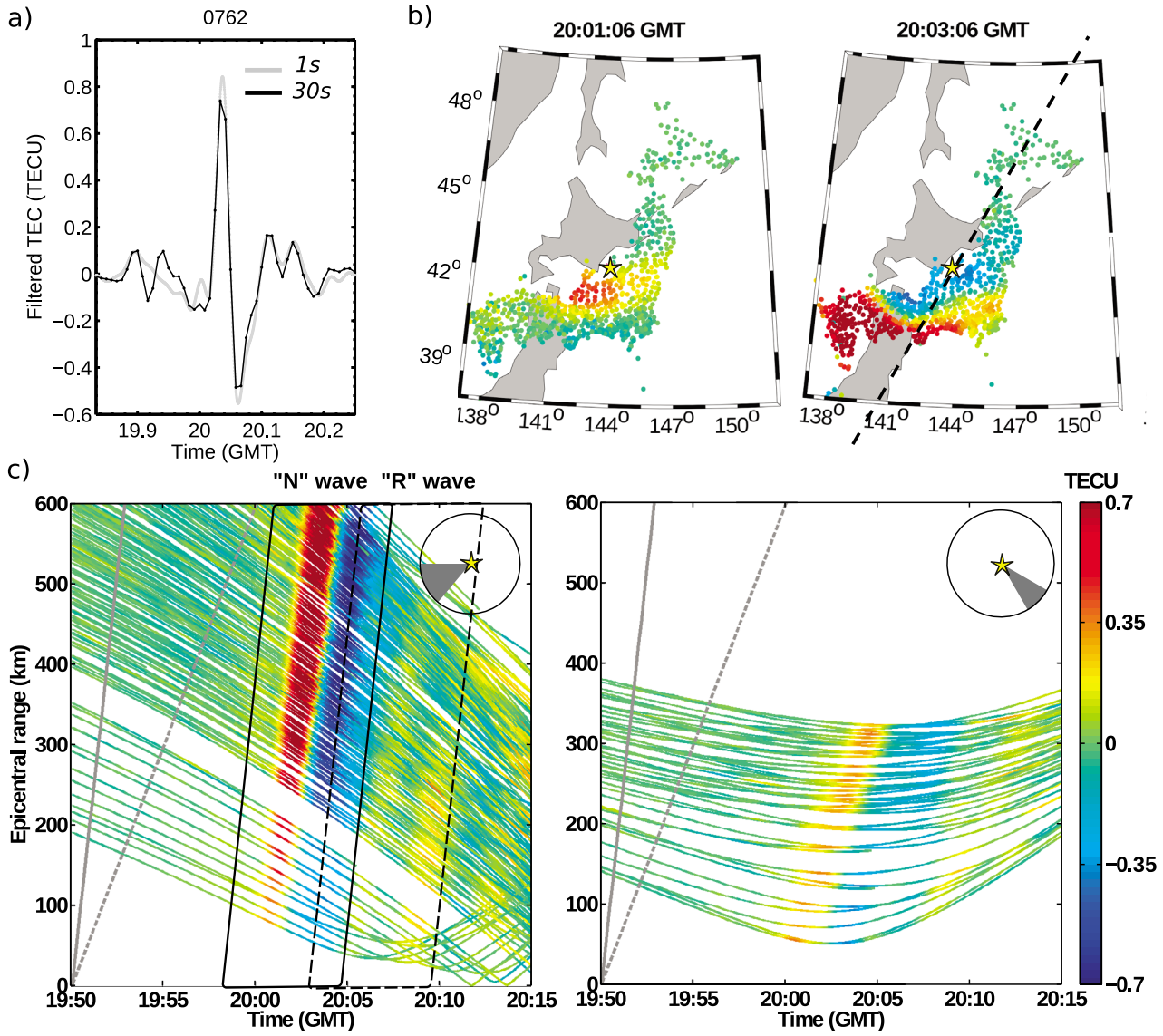

Figure 4. (a) Example of filtered slant TEC time series (1–10 mHz frequency band), with sampling at 1 s and 30 s in grey and black, respectively. (b) Filtered TEC maps measured 11 and 13 min after the Tokachi-Oki earthquake. The estimated origin time is 1950:06 UT. Each point (IPP) corresponds to a pair formed by a GEONET GPS ground station and GPS satellite 13 and is located at 300 km height for representation purpose. The star locates the epicenter. We present snapshots from 10 to 20 min after the earthquake in Animation S2 in the auxiliary material. (c) Traveltime diagram of the filtered slant TEC with azimuthal selection of the IPPs. (left) Western IPP selection (azimuth from 220° to 360°). The "N" wave (outlined with a plain line) is the acoustically resonant component of the Rayleigh driven perturbation while the "R" wave (outlined with a dashed line) is the seismic component that we model. (right) Eastern IPP selection (azimuth from 130° to 150°).

[11] In order to extract the TEC, we use the phase measurements of the two carrier frequencies (f_1 = 1575.42 MHz and f_2 = 1227.60 MHz). Biased slant TEC (STEC) time series are computed for each satellite-station pair from the L_1 and L_2 carrier phases difference following *Mannucci et al.* [1998] and *Lognonné et al.* [2006]. Short-term ionospheric perturbations are extracted by removing the long-period variations due to the ionospheric daily variability, satellites motion and to the quasi-constant instrumental biases. Data are, therefore, detrended and band-pass filtered between 1 and 10 mHz by a Butterworth filter.

[12] High-rate (1 Hz sampled) GPS data were provided by the GSI for the Tokachi-Oki event. They have two advantages: first, they are less noisy as compared to 30 s sampled data [*Crespon*, 2007], which lowers the detection threshold. Second, they sample high-speed Rayleigh wave induced ionospheric waves better, especially for dense networks, where the propagation time between two GPS stations is less than 10 s.

[13] For each satellite-receiver pair, the observed or modeled time-filtered STEC (dSTEC) values are associated with the ionospheric pierce point (IPP). The IPP is the intersection point of the satellite-receiver raypath with a 300 km thin

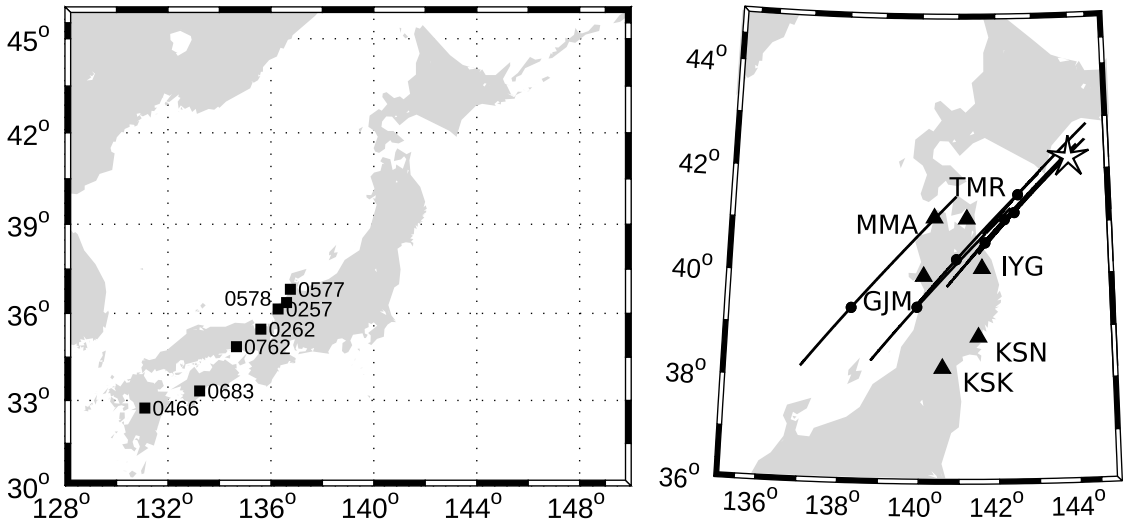

Figure 5. (right) Selection of satellite 13 IPP tracks crossing southwest from the Tokachi-Oki earthquake epicenter between 1950 and 2015 UT. Dots indicate the locations of the IPPs at 2000 UT. Triangles indicate the location of nearby broadband seismometers. (left) The locations of the corresponding ground receivers.

shell, and therefore, is moving with time with the GPS satellite. However, this representation is not associated with any 2-D thin shell approximation of our modeling and is used only for the purpose of signal description. Despite a very irregular and moving sampling, the density of the wide Japanese GPS array allows the direct imaging of coseismic ionospheric waves, characterized by wavelengths ranging from 100 to 300 km. In the following, we will use the denomination "TEC map" for the filtered STEC perturbation mapped at IPPs at a given time.

3. Observations

[14] Using the very dense GPS network GEONET, we focus on the observations and the modeling of GPS TEC Rayleigh wave induced ionospheric waves observed at far field and at near field: after the 2008 Wenchuan earthquake and after the 2003 Tokachi-Oki earthquake, respectively.

3.1. Events Characteristics

[15] The earthquake parameters used in our simulations were first based on the centroid moment tensor (CMT) of Columbia University (http://www.globalcmt.org/) and values are reported in Table 1. Tectonic information is from the U.S. Geophysical Survey (http://earthquake.usgs.gov/).

[16] The $M_w = 7.9$ ($M_s = 8.1$) Wenchuan earthquake occurred in midafternoon (1428:01 LT at epicenter, 0628:01 UT), on the northwestern margin of the Sichuan Basin and 90 km from Chengdu, the Sichuan capital (104.10°E; 31.44°N). This destructive earthquake resulted from the rupture of a northeast thrust fault (strike 231°) at a focal depth of 12.8 km. The near-field TEC signal was analyzed by *Afraimovich et al.* [2010]. It is characterized by an N-shaped acoustic wave, with a wavefront parallel to the earthquake rupture direction and a clear southeastward emission lobe. Data in the far field were, however, not studied. The GPS GEONET network allows such observations southeast of the epicenter at epicentral distances of 1500–2000 km.

[17] The M_w = 8.3 (M_s = 8.1) Tokachi-Oki earthquake was a shallow interplate earthquake with a hypocenter depth of 28 km. The rupture occurred 60 km from the Hokkaido island east coast (143.84°E; 42.21°N), at nighttime (0450:06 LT, 1 day ahead at epicenter, 1950:06 UT). The thrust fault ruptured northwestward (strike 250°) at an average phase velocity reaching the shear wave velocity (4.5 km/s) and a 6 m maximum slip was estimated by *Yagi* [2004]. The rupture generated strong long-period vertical displacements [*Aoi et al.*, 2008], favorable to an efficient coupling with the atmosphere. Both coseismic neutral atmospheric waves and therefore, ionospheric waves are reported. The first are illustrated by the pressure waves observations of Rayleigh wave induced atmospheric waves that propagate at a velocity of 3.2 km/s [*Watada and Kanamori*, 2010]. The latter were near-field TEC disturbances investigated by *Heki and Ping* [2005]. We focus the paper on the Rayleigh wave induced ionospheric TEC observations.

3.2. Far-Field Observations: Wenchuan

[18] Shortly after the Wenchuan earthquake, ionospheric waves were detected by satellite 14, traveling eastward and reaching the east of Japanese archipelago, as shown by Figure 3. The ionospheric perturbations in the south, over the East China Sea, have maximum amplitudes of 0.15 TECU in the 1 to 10 mHz frequency bandwidth. The propagation velocity can be obtained directly from the amplitudes of the TEC, represented as functions of both time and epicentral

Table 2. The 1-D Atmospheric Model Input Parameters[a]

Seismic Event	Time (UT)	Local Time	Location (Lon/Lat)	F10.7/ F10.7a
Wenchuan	0648	1548	30°N/122°E	68.0/68.3
Tokachi-Oki	2000	0500	42°N/144°E	133.5/131.9

[a]F10.7 and F10.7a denote the solar flux index, daily and averaged over 80 days, respectively.

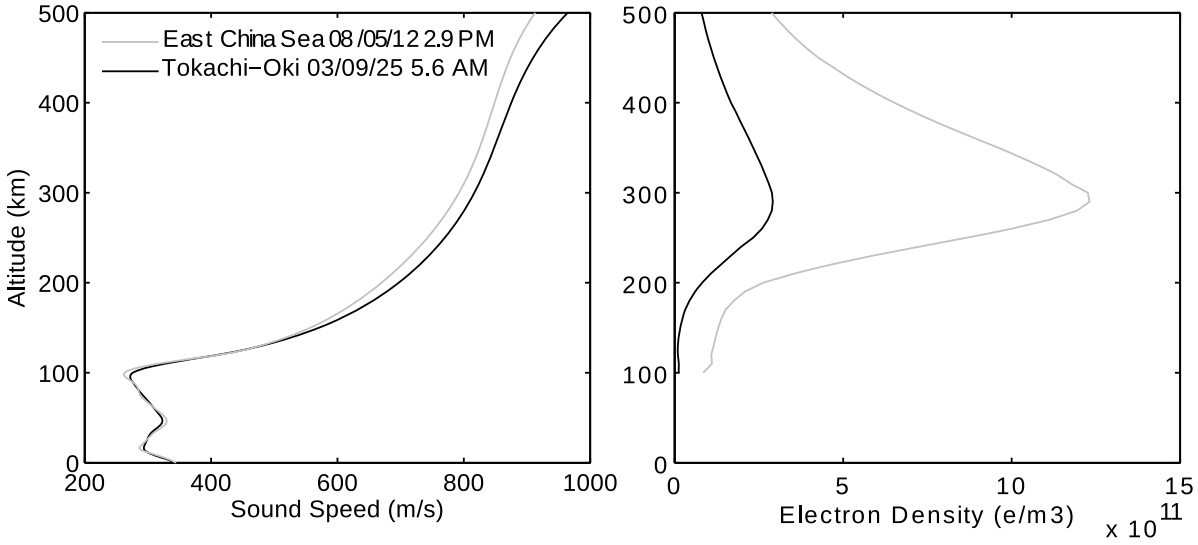

Figure 6. Sound speed and electron density profiles derived from the NRL-MSISE00 model and IRI 2007 model, respectively, for the two events investigated in the paper.

distance. Figure 3 shows the filtered TEC time series as function of the IPP epicentral distance for satellite 14.

[19] The signal-to-noise ratio is relatively low. This is probably related to the observation time (local midafternoon) and to the 30 sec sampling rate of the data. Nevertheless, a coherent signal is found, highlighted by a stack of the first perturbed STEC time series, each of them shifted by the time shift found by cross correlation (see *Dučić et al.* [2003] for methodology details). It results in a N-shaped wave, with a broad peak frequency around 5 mHz. However, no significant perturbation is detected by the other visible satellites presented in Figure 2. The IPPs of satellite 14 have a low elevation angle of around 30°, while the IPPs of satellite 22 crossing close by have a 50° elevation angle approximately. This shows a high sensitivity to the elevation angle. A southeastward directivity seems also to be observed in this far field, as for the near field after *Afraimovich et al.* [2010]. This directivity is confirmed by the analysis of the GPS observations of satellite 14. Indeed, IGS (International Global navigation satellite system Service) station PIMO located in the Philippines shows that 1975 km away from the epicenter right to the southeast the amplitude of the "N" wave is 0.15 TECU while at the same distance right to the east the amplitude measured by the GEONET GPS station 0733 is 0.08 TECU.

3.3. Near-Field Observations: Tokachi-Oki

[20] As reported by *Heki and Ping* [2005] strong N-shaped coseismic ionospheric disturbances are detected with the GEONET network within 10 min after the Tokachi-Oki earthquake. This work provided a complete description of the observation geometry, summarized in Figure 2. An acoustic pulse is detected with the almost vertical satellite 24 and Rayleigh wave induced TEC perturbations are detected with satellite 13. Again, the elevation angle is low (about 30°) and Rayleigh waves are also observed on the sounding points close from the epicenter. The "N" wave is shown in

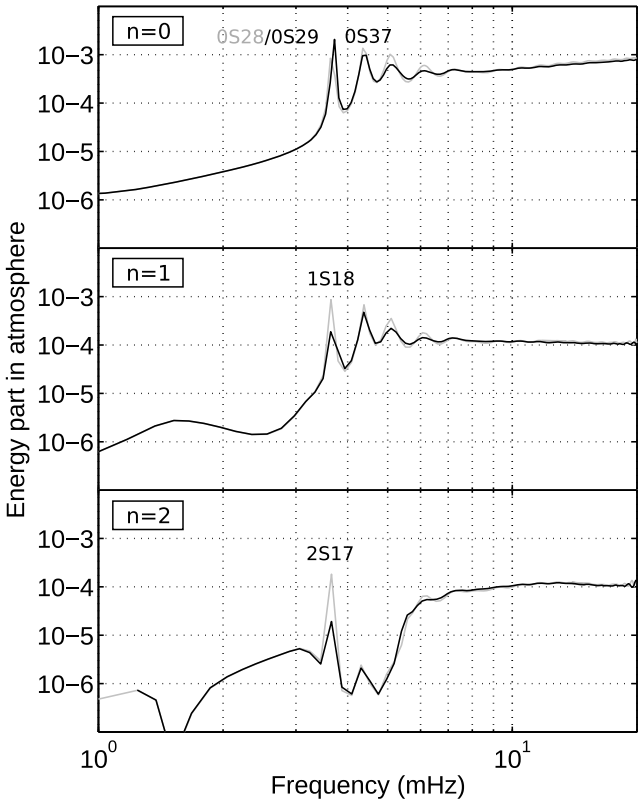

Figure 7. Relative energy of the solid Earth modes injected in the atmosphere, between 0 and 20 mHz. The fundamental modes and two first overtones are shown for the Tokachi-Oki earthquake in black and for the Wenchuan earthquake in gray. They are computed with a radiative boundary condition, and the viscosity is taken into account. Note the resonance at 3.7 and 4.3 mHz.

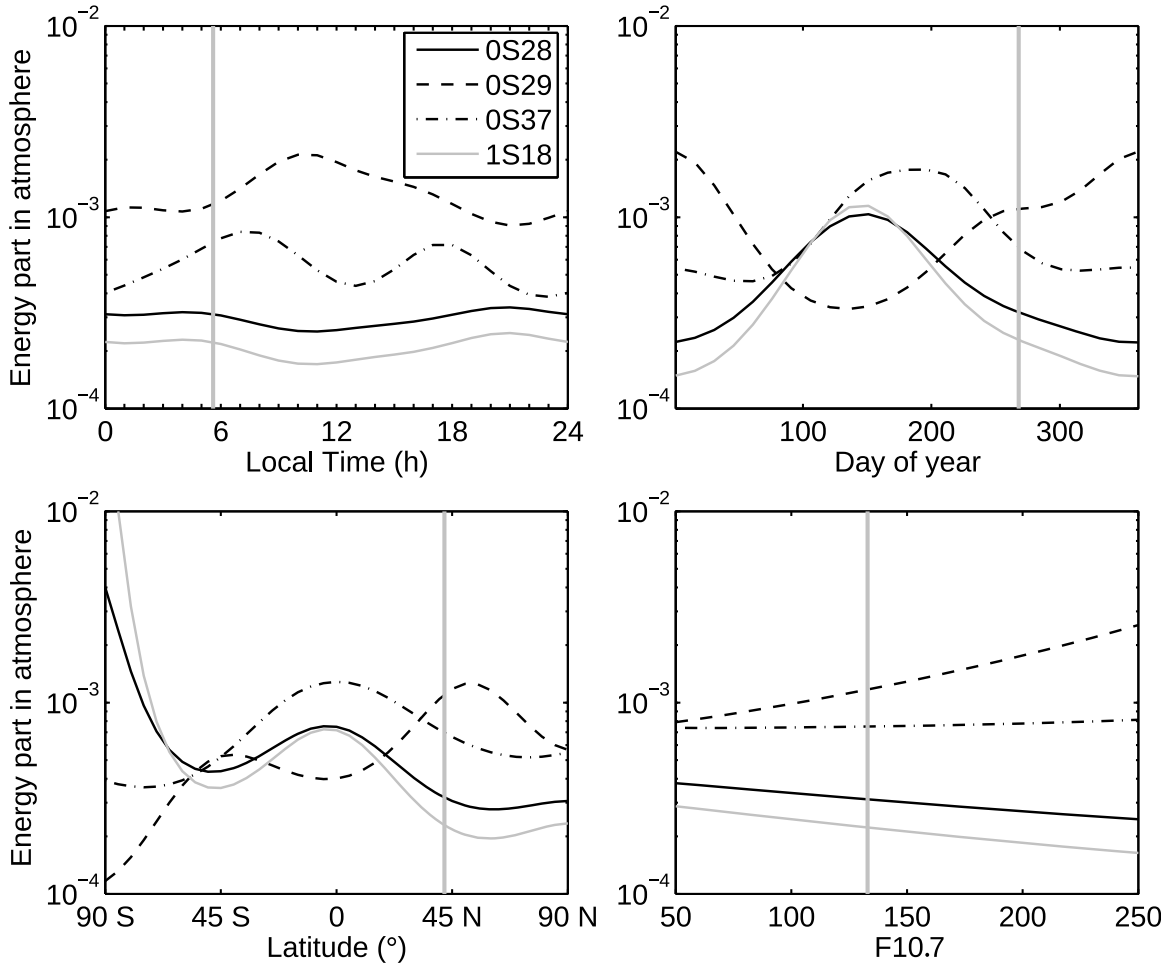

Figure 8. Variability of the solid Earth–atmosphere coupling at the Tokachi-Oki earthquake epicenter as function of local time, day of year, latitude, and solar flux F10.7. The part of the energy injected in the atmosphere is plotted for the first resonant solid modes ${}_0S_{28}$, ${}_0S_{29}$, ${}_0S_{37}$, and ${}_1S_{18}$ (see Figure 7). The default parameters used for the atmospheric model are given in Table 3, and for each variability plot the parameter used for the Tokachi-Oki event is marked by a vertical line.

Figure 4a. Note that the 1 s sampling is better suited than the 30 s sampling. Two TEC maps measured with satellite 13 are shown in Figure 4b and the whole perturbation pattern can be seen in Animation S2 provided in the auxiliary material.[1] On Figure 4b (left), a perturbation appears about 10 min after the main shock. On Figure 4b (right), a pattern with a nodal line can be observed, about 13 min after the main shock. The azimuth of this nodal line is 210 ± 20°, comparable to the azimuths of the first fault plane determined by global CMT project (250°), U.S. Geophysical Survey (234°) and the Russian National Seismological Center (190°) [*Crespon*, 2007]. As a consequence, we can suppose that this specific pattern is directly related to the seismic rupture.

[21] As also shown by Figure 4b, the IPPs of satellite 13 sound the epicenter area with a wide range of azimuths. In order to avoid the overlapping of the IPPs tracks on traveltime diagrams, we made an azimuthal selection of the IPPs. Figure 4c shows two distinct propagation speeds: on the east, the whole perturbation propagates with a slope close to 1 km/s, which corresponds to the sound speed near F2 peak. Therefore, these waves are associated with the acoustic plume produced by the direct piston-like effect on the atmosphere, as acoustic rays are deflected at F2 altitudes and when the line-of-sight integrations are maximal. These waves were also observed by the satellite 24 [*Heki and Ping*, 2005].

[22] On the west, the propagation speed is larger than 3 km/s right above the epicentral region. Those fast speed waves are induced by the Rayleigh waves propagating at the Earth's surface at nearly 3.5 km/s. The first perturbation is a N wave with an amplitude of 1 TECU peak to peak in average and a 4 to 5 min period (i.e., 3.3 to 4.2 mHz). It is followed by a weaker oscillatory signal, with an amplitude not exceeding a few tenths of TECU peak to peak [see *Heki and Ping*, 2005, Figure 3]. Therefore, we propose a model of the near-source three-dimensional ionospheric Rayleigh pattern aiming to explain the oscillatory signal and to relate the observations to the focal mechanism. We will particularly focus on a selection of IPP tracks traveling southwestward from the epicenter as presented in Figure 5.

[23] *Heki and Ping* [2005] also noticed that the TEC signal-to-noise ratio is very low at the northeastern IPPs.

[1] Auxiliary materials are available in the HTML. doi:10.1029/2010JA016060.

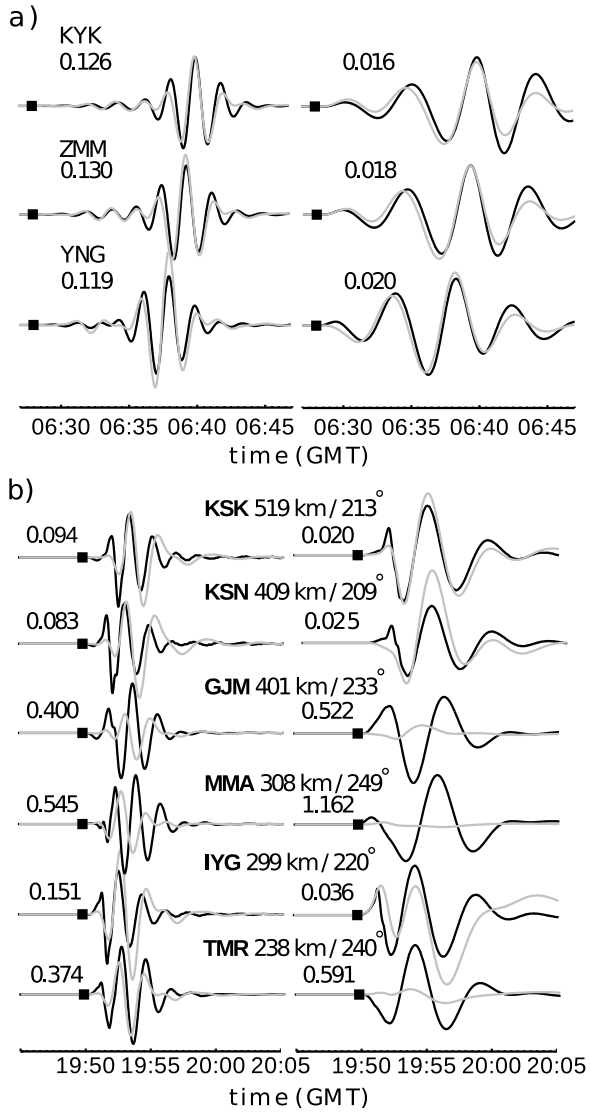

Figure 9. Normalized vertical component of the ground velocity measured by selected seismometers of the broadband network FNET (black curves) compared to synthetics seismograms modeled using normal modes summation with point source approximation (gray curves). The maximum amplitude of the measured perturbation is indicated in mm/s. (a) Seismograms for the Wenchuan earthquake, filtered from 1 to 10 mHz. (b) Seismograms for the Tokachi-Oki earthquake; the seismograms on the left are filtered from 4 to 10 mHz, while they are filtered from 1 to 4 mHz on the right. The black squares mark the seismic origin times. The seismometers used for Figures 9a and 9b are marked on Figures 3 and 5, respectively. Note the particularly strong long-period motions measured by seismometers TMR, MMA, and GJM for the Tokachi-Oki event.

Such directivity was already observed by *Calais et al.* [1998], who suggested an origin related to geomagnetic field effects.

4. Modeling

[24] We computed the perturbation by the following sequential scheme: we first model the atmospheric wave by summation of the normal modes. Through neutral-plasma coupling we model the coupled electronic perturbation. Finally, we integrate the electron density to obtain the perturbed TEC. The second step includes the effect of the magnetic field, whose importance is now confirmed by several ionospheric observations. We are, therefore, not only using a rigorous modeling of the Rayleigh waves by normal modes summation, but also do a full ionospheric coupling modeling of the momentum transfer between the neutral atmosphere and the ionosphere in the Earth's magnetic field, using the formalism described by *Occhipinti et al.* [2008] and *Kherani et al.* [2009]. See a similar approach for the near-source perturbation associated with the eruption of the Montserrat volcano [*Dautermann et al.*, 2009]

4.1. Normal Mode Computation

[25] Several equivalent methods have been dedicated to the computation of normal modes with atmosphere [*Lognonné et al.*, 1998; *Kobayashi*, 2007; *Watada et al.*, 2006], but so far none with source freely distributed, in contrary to normal modes and synthetic seismograms [*Woodhouse*, 1988; *Clévédé and Lognonné*, 2003]. We have used the one developed by our team, which includes viscosity in the atmosphere [*Lognonné et al.*, 1998; *Artru et al.*, 2001]. However, none of these methods includes the other source of atmospheric attenuation, such as thermal conduction and the collisions of ions on neutral particles [e.g., *Hickey et al.*, 2009]. Therefore viscosity must be considered as an ad hoc parameter, which takes all these effects into account. Lateral and time variations in the atmospheric and ionospheric parameters are also only locally modeled by using an atmospheric model without winds, corresponding to the atmosphere sensed by the propagating waves. This assumption is robust for the almost vertically propagating Rayleigh waves studied in this paper but probably weaker for the acoustic long distance propagating waves emitted directly by the earthquake or in low-latitude regions, where the magnetic field is perpendicular to the neutral atmosphere velocity and ionosphere coupling significant [*Hickey et al.*, 2009].

[26] The fundamental Rayleigh spheroidal modes and the 10 first overtones (eigenmodes and eigenfrequencies) of an anelastic Earth surrounded by a realistic one-dimensional atmosphere are computed following the method proposed by *Lognonné et al.* [1998] up to 20 mHz. This corresponds to a maximum angular order $\ell = 203$.

[27] Our method, with examples of applications of *Artru et al.* [2001, 2004] and *Dautermann et al.* [2009], consists in two steps. First, a complete set of normal mode functions is computed for an elastic Earth model and a free surface using the Minos software [*Woodhouse*, 1988] which solves the elastodynamic equation in the frequency domain. The Earth model used is the one-dimensional (1-D) anisotropic Preliminary Reference Earthquake Model [*Dziewonski and Anderson*, 1981]), and the surrounding 500 km thick 1-D atmosphere is modeled by the NRLMSISE-00 model [*Picone et al.*, 2002]. The atmospheric parameters (air density and sound speed) and solar parameters (F10.7 index) were computed at the time and location of the observations, to account for the dependency of the coupling efficiency with local time [*Lognonné*, 2009], as given by Table 2. The sound speed profiles calculated for both events are shown in Figure 6.

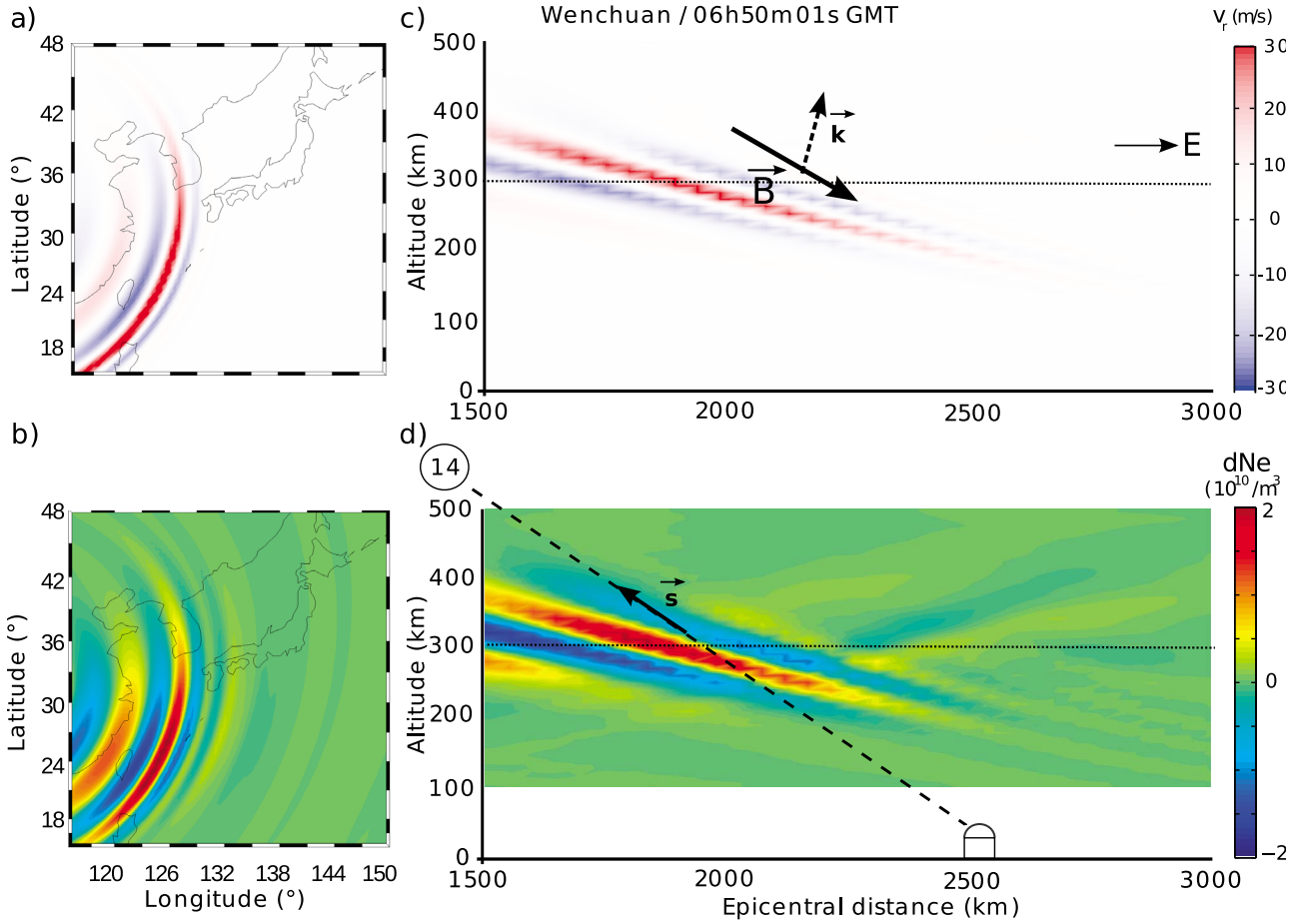

Figure 10. Modeling of Rayleigh wave induced atmospheric and ionospheric waves 22 min after the Wenchuan earthquake. (a and b) Horizontal slices at 300 km of the vertical component of the neutral velocity perturbation u_r and of the electron density perturbation δN_e, respectively. (c and d) Vertical slices along the dotted line depicted in Figures 10a and 10b of u_r and δN_e, respectively. The **k** is the wave vector, **B** is the geomagnetic field vector, and **s** is the observation vector, which is the direction vector of the line of sight of a receiver-satellite couple. Note that for satellite 14, **s** is almost perpendicular to **k**, which means a constructive integration of the electron density perturbation.

[28] Second, a radiation boundary condition is imposed at the top of the atmosphere to model the attenuation of the acoustic waves at larger altitudes. For acoustic waves, the atmospheric attenuation due to viscosity cannot be neglected and is included following *Artru et al.* [2001].

[29] The normal modes are then solved through a variational method. Solutions are new complex eigenmodes and eigenfrequencies. Figure 7 shows the part of the energy injected in the atmosphere for the fundamental branch and the two first overtones of Rayleigh solid modes. The relative energy of the fundamental branch is also computed without viscosity. This highlights the increasing attenuation effect on modes with the increasing frequency.

[30] Solid modes couple efficiently with the atmosphere when their eigenfrequencies are close to the frequencies of the atmospheric waveguides. The most energetic atmospheric modes are trapped in the low altitude atmospheric waveguide at frequencies 3.7 mHz and 4.3 mHz [*Lognonné et al.*, 1998]. Depending on the atmospheric conditions, solid modes ${}_0S_{28}$ (Wenchuan case) or ${}_0S_{29}$ (Tokachi-Oki case) are alternatively resonant at about 3.7 mHz. Mode ${}_0S_{37}$ is resonant at 4.4 mHz. The coupling is more efficient when the frequencies of the atmospheric fundamental acoustic modes ${}_0P_{28}/{}_0P_{29}$ and ${}_0P_{37}$ get closer to the solid Earth Rayleigh fundamental normal modes ${}_0S_{28}/{}_0S_{29}$ and ${}_0S_{37}$, respectively. The same is observed for the overtones, as shown by resonances at ${}_1S_{18}$ and ${}_2S_{17}$ on Figure 7. The lower-frequency resonance computed for the Wenchuan case as compared to the Tokachi-Oki case (i.e., ${}_0S_{28}$ compared to ${}_0S_{29}$) can be understood from the speed profiles on Figure 6, which shows a slightly larger waveguide due to the upward extension of the mesopause above 100 km of altitude and therefore a better resonance with the lower-frequency ${}_0S_{28}$ mode.

[31] The variation of the atmospheric energy of resonant modes with variable atmospheric conditions is shown on Figure 8. Coupling between the Solid Earth and its atmosphere appears to be most energetic at noon and during the solstices, when the solar heating is the most intense. This tendency is confirmed by the linear growth of the resonant mode ${}_0S_{29}$ energy with increasing solar flux F10.7. The role of this last parameter is however smaller than the

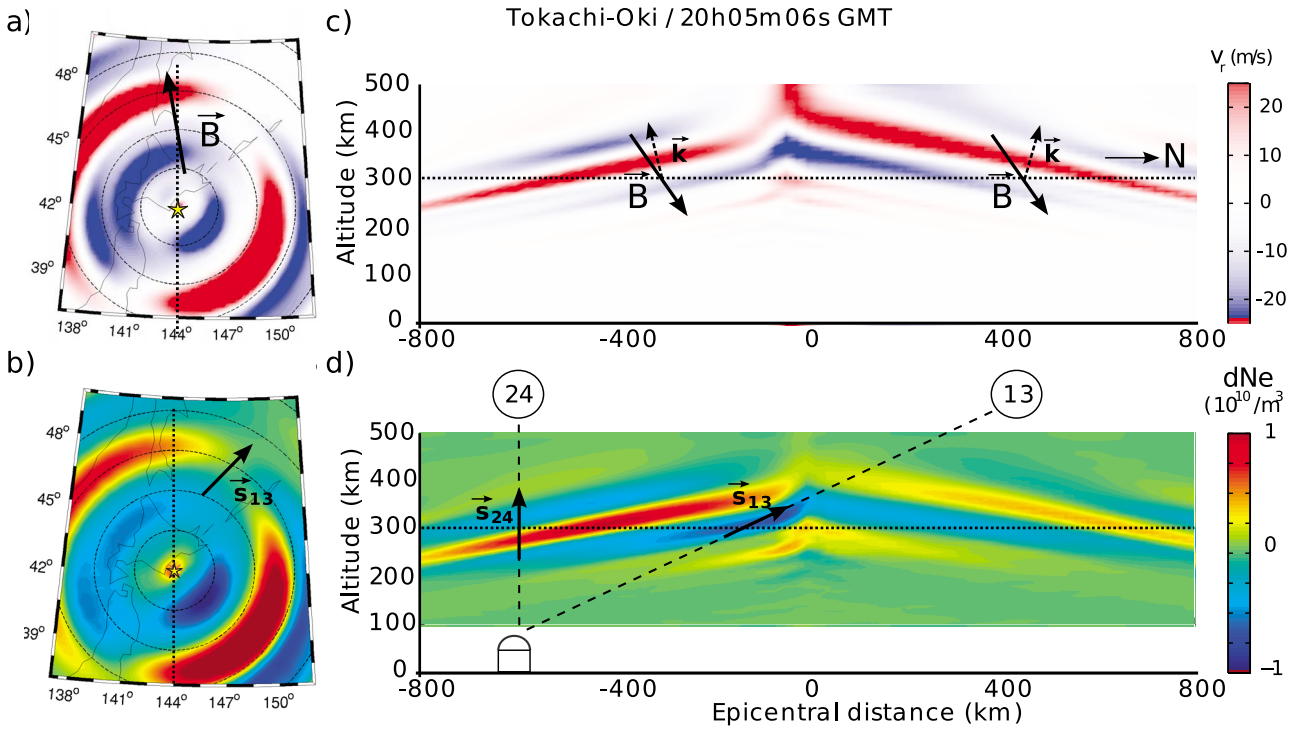

Figure 11. Same as Figure 10 but 15 min after the Tokachi-Oki event. The geomagnetic inclination at epicenter is about 55°. With satellite 13, the integration of the electron density perturbation is constructive in the southwest and destructive in the northeast, while it is fully destructive with satellite 24.

local time and the day of year. The latitudinal variations are more complex, combining seasonal variations with the inclination of the Earth with respect to solar light, which is probably generating the large magnification modeled in the Southern Hemisphere.

[32] As a consequence and despite the lower F10.7 solar flux, the coupling is more efficient for the Wenchuan case, at early afternoon and end of May than for the Tokachi-Oki case, at nighttime and end of October (see Table 2).

4.2. Seismogram Computation

[33] The excitation of the Earth's normal modes by the seismic rupture is modeled in a standard way by a double couple applied to a point source. Before computing the ionospheric response, we want to quantify the modeling error due to this source and solid earth models on the ground vertical velocity field, which will automatically propagate in our ionospheric modeling. For this purpose, we compute seismograms with the same approach and compare them to data recorded by the Japanese broadband seismometers network FNET.

[34] Assuming a Heavyside time source function (H(t)), the displacement $\mathbf{s}(\mathbf{r}, t)$ is expressed after *Lognonné* [1991] at any point $\mathbf{r}$ as

$$\mathbf{s}(\mathbf{r},t) = H(t)\Re e\left[\sum_k \mathsf{M} : \boldsymbol{\epsilon}_k(\mathbf{r}_0)\ \mathbf{u}_k(\mathbf{r})\ \frac{1-e^{i\sigma_k t}}{\sigma_k^2}\right], \qquad (1)$$

where M is the moment tensor (we use global CMT), $\mathbf{r}_0$ is the source location, ϵ_k is the deformation associated with the eigenmode $\mathbf{u}_k$ with eigenfrequency σ_k, and $\Re e$ denotes the real part. The amplitude of equation (1) are then convoluted by the source time function and when compared to seismograms, by the response function of the instruments. The source time function is a boxcar having a half duration htc and delayed by a time shift dtc given in Table 1. Note that we do not take here into account the change in the convention of the CMT method after the 1st January 2004, as it uses a triangular source time function to estimate the source parameters of the events that occurred after. For the 2008 Wenchuan earthquake case, the error made using a boxcar function is lower than 10% in amplitudes, as we focus only on long periods.

[35] For consistency, we first model the vertical coseismic motions at ground level at the locations of selected broadband seismometers of the network FNET (see locations in Figures 3 and 5) and compared them to the data provided by the public Web site http://www.fnet.bosai.go.jp. As shown by Figure 9, the seismograms are well reproduced through normal modes summation technique at far field in the 1 to 10 mHz frequency range. At near field, the point source approximation provides synthetics in rather good agreement with the data in the 4 to 10 mHz frequency range but fails to reproduce the long-period ground motions observed by seismometers GJM, MMA and TMR from 1 to 4 mHz. For these seismic stations, the observed amplitude is more than 20 times larger as for the other stations. This lack of long-period ground motion, either due to the more complex and finite sources or to 3-D lateral variations in the crust and possible sedimentary resonances, must be kept in mind for further comparison of the TEC data and synthetics.

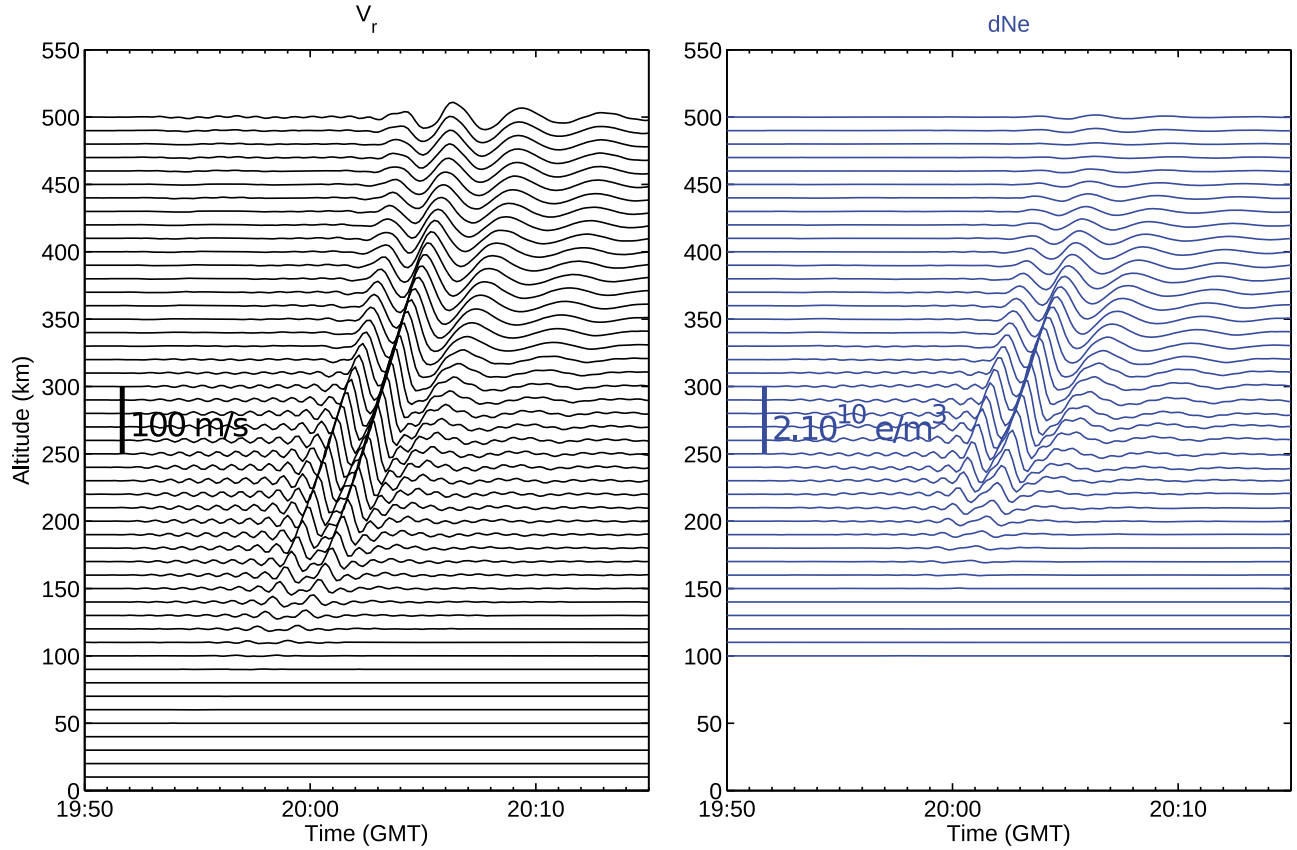

Figure 12. (left) Vertical oscillations in velocity (V_r) of the neutral atmosphere modeled by normal modes summation at 140.4°E and 41.2°N for the Tokachi-Oki earthquake case, as function of time and altitude. (right) Corresponding perturbation of the electron density (dNe) modeled by ionospheric coupling.

4.3. Neutral-Plasma Coupling

[36] The first step to model the coupling is the computation of the velocity wavefield or 3-D "wind" maps of the neutral atmosphere. For this purpose, synthetic seismograms in velocity $\mathbf{u}(\mathbf{r}, t) = d\mathbf{s}(\mathbf{r}, t)/dt$ are computed for the three components (vertical, south and east) at each node of the spherical grid in the atmosphere. This three-component field extends from 100 to 500 km in altitude, with an horizontal spacing of 0.2 degree both in longitude and latitude (a maximum of 25 km horizontal space step corresponding to about 1/7 of the Rayleigh wavelength at 20 mHz and 3.5 km/s horizontal propagation speed). The vertical spacing is 10 km, corresponding to 1/4 of the Rayleigh wavelength at 20 mHz and 0.8 km/s vertical propagation speed. Instantaneous vertical velocity patterns are presented on Figures 10 and 11).

[37] We applied a finite difference scheme to solve the transport and continuity equations of ions [*Kherani et al.*, 2009], using a time step of 10 s. A comparative test with a vertical space step of 5 km and a 5 s time step shows a residual lower than 10% on the final perturbed TEC value. As a consequence, a 10 km vertical space step and a 10 s time step are chosen, as they provide a sufficiently accurate result in a reasonable computation time.

[38] The ionospheric (electron density N_e), geomagnetic field and transport parameters (ion collision frequencies ν_{in}) are computed at the time and location of the earthquake on the whole modeling grid using the International Reference Ionosphere (IRI) [*Bilitza and Reinisch*, 2008], the International Geomagnetic Reference Field (IGRF-10) [*Maus et al.*, 2005] and SAMI2 [*Huba et al.*, 2000], respectively.

Table 3. Overview of the Significant Rayleigh Wave Induced Ionospheric Observations Made by GPS TEC Technique[a]

Date	Epicenter Location	M_s	Satellite	δSTEC (TECU)	El (deg)	Reference
3 Nov 2002	Denali	8.5	26	0.05	25	*Dučić et al.* [2003]
26 Dec 2004	Sumatra	8.9	13	0.05	40	*Occhipinti* [2006]
12 May 2008	Wenchuan	8.1	14	0.1	30	this paper
4 Oct 1994	Kuril islands	8.1	06	0.3	40	*Astafyeva et al.* [2009]
25 Sep 2003	Tokachi-Oki	8.1	13	0.7	40	this paper
15 Nov 2006	Kuril islands	8.3	20–13	0.2	30	*Astafyeva and Heki* [2009]

[a]The maximum peak to through amplitude of the filtered slant TEC δSTEC (in TECU) and the associated earthquake characteristics (M_s is the surface wave magnitude) and observation geometry with the observed satellite elevation angle El are given.

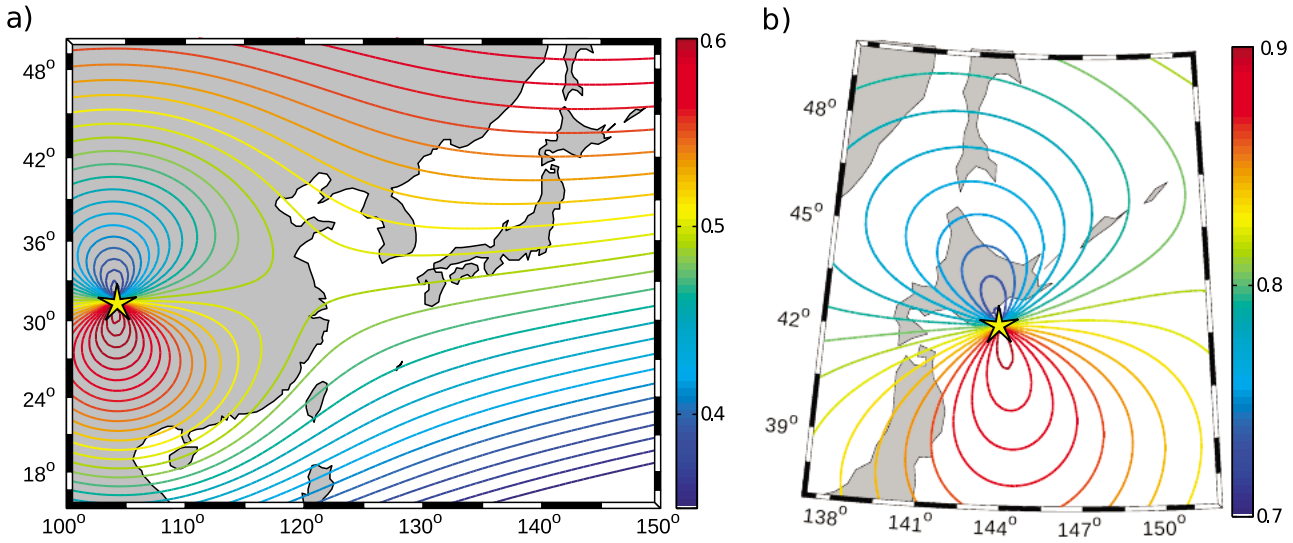

Figure 13. Ionospheric coupling factor α modeled for a Rayleigh induced atmospheric wave generated at the epicenter of (a) the Wenchuan earthquake and (b) the Tokachi-Oki earthquake. We follow equation (4), with wavefronts having a constant 10° inclination and the local geomagnetic field modeled at 300 km height.

[39] We use the formula established by *McLeod* [1966]:

$$\mathbf{v}_i = \frac{1}{1+\kappa^2}\left[\kappa^2\mathbf{u} + \kappa\mathbf{u}\times\mathbf{1}_b + (\mathbf{u}\cdot\mathbf{1}_\mathbf{b})\mathbf{1}_\mathbf{b}\right], \tag{2}$$

where $\mathbf{1}_b$ is the unit vector of the geomagnetic field having intensity B, $\kappa = \nu_{in}/\Gamma_i$ is the ratio of the neutral ion collision frequency to the ion gyrofrequency $\Gamma_i = q_iB/m_i$, where B denotes the geomagnetic field intensity and q_i, m_i are the charge and mass of ions. As the collision frequency is decreasing with altitude, the κ parameter can be neglected in the F region. *Hooke* [1970] simplified the expression for perturbations at midlatitude and F region ($\kappa \to 0$):

$$\mathbf{v}_i = (\mathbf{u}\cdot\mathbf{1}_b)\mathbf{1}_b. \tag{3}$$

So the ion velocity induced by the neutral particles motion is mostly proportional to α, that is the cosine of the angle between the neutral velocity and geomagnetic field vectors [*Hooke*, 1970] and known as the ionospheric coupling factor [*Calais et al.*, 1998]:

$$\alpha = \mathbf{k}\cdot\mathbf{1}_b, \tag{4}$$

where $\mathbf{k}$ is the atmospheric perturbation wave vector.

[40] The electron density fluctuations are derived from the continuity equation for ions:

$$\frac{\partial N_e}{\partial t} + \nabla\cdot(N_e\mathbf{v}_i) = 0. \tag{5}$$

After linearization, assuming that the fluctuations are small: $N_e(t, \mathbf{r}) = N_{e0} + \delta N_e(t, \mathbf{r})$, we integrate the continuity equation:

$$\delta N_e(t,\mathbf{r}) = -\int_0^t \nabla\cdot(N_{e0}\mathbf{v}_i(t,\mathbf{r}))dt. \tag{6}$$

[41] The resulting instantaneous ionospheric patterns are presented in Figures 10 and 11. To be more specific, Figure 12 shows an example of the modeled atmospheric and ionospheric seismograms as function of altitude. The vertical neutral velocity perturbation is 0.4 mm/s peak to peak at ground level and as expected, increases exponentially with the altitude as the air density decreases, reaching a maximum at 280 km height, with 120 m/s peak to peak at this location, then decreases by viscous damping. Note also the low-pass filtering effect of the increasing viscosity. The maximum perturbation in electron density is reached at 290 km height, close to the F2 peak height, with a peak-to-peak amplitude of 1.7×10^{10} electrons per m^3. This corresponds to nearly 5% of the unperturbed plasma density.

[42] The resulting 3-D perturbed electronic density is finally integrated along each satellite-receiver path (shown in Figures 10 and 11), using the IGS orbit ephemeris.

5. Results and Discussion

5.1. Source Effect

[43] The atmospheric Rayleigh wave radiation patterns are shown in Figures 10 and 11 for the Wenchuan and Tokachi-Oki earthquakes, respectively. Both earthquakes induce a southeastward directivity in the emission lobes of the Rayleigh wave radiation pattern. The vertical slices also show the characteristic conic-like geometry. Indeed, Rayleigh wave induced waves are launched in the atmosphere with an elevation angle given to the first order by the Snell-Descartes law. As the ratio between the Rayleigh surface-waves phase velocity and the sound speed at the ground is about 10, the elevation angle of the atmospheric wavefront at the ground is slightly less than 6°. It increases progressively to reach about 14° at 300 km of altitude, where the sound speed reaches about 800 m/s (as compared to about 3500 m/s for the Rayleigh waves). As shown by Table 3, which lists past published observations, the integration of

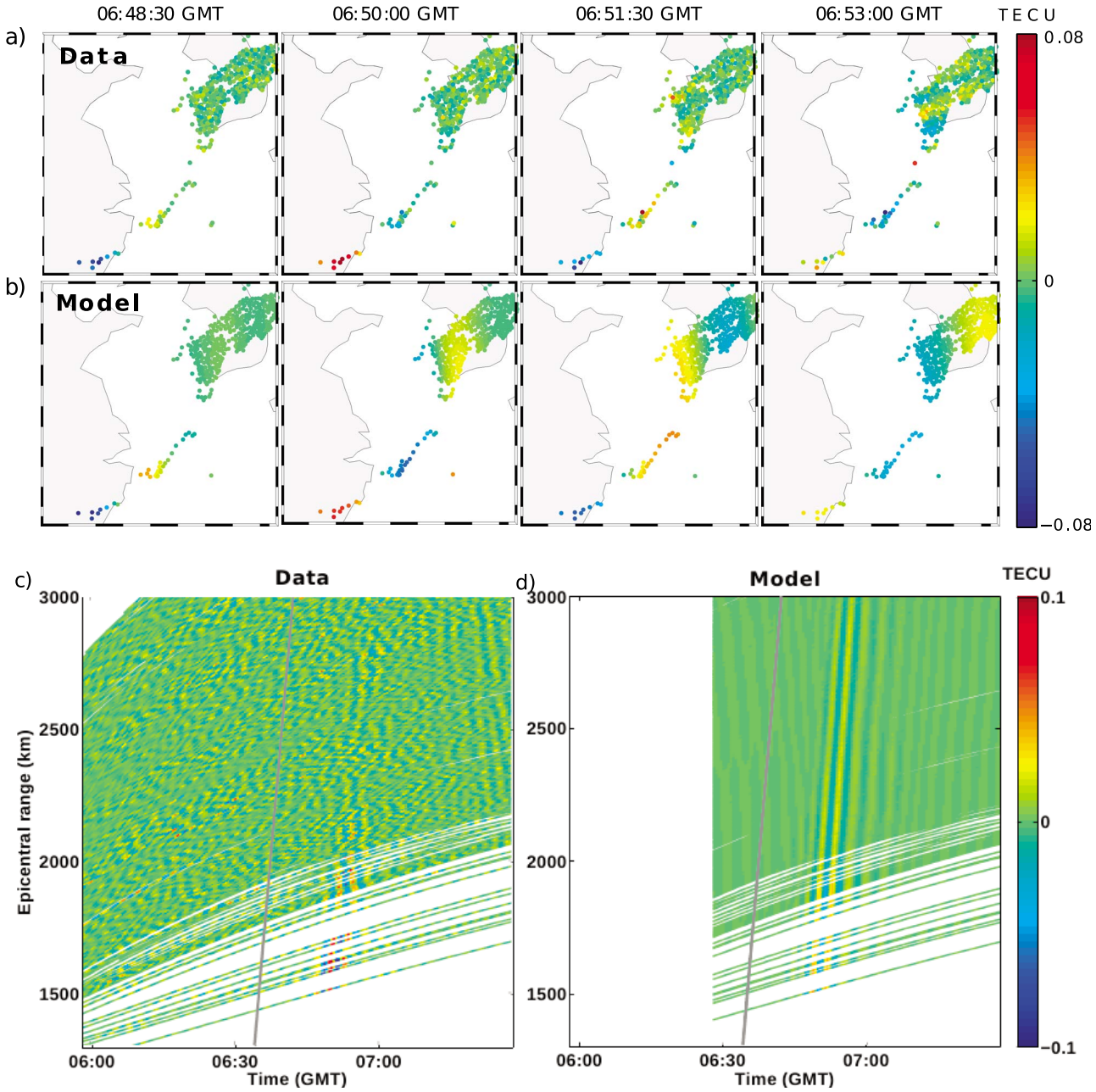

Figure 14. (a) Filtered TEC at IPPs measured by GEONET and the satellite 14 after the Wenchuan earthquake. (b) The corresponding synthetics. (c and d) Measured and modeled travel time diagram. Time series are filtered between 4 and 10 mHz.

the oscillating perturbations requests a low elevation angle in order to be significantly nonzero: practically, only satellites with elevation angle lower than 40° provide an efficient detection of Rayleigh wave induced ionospheric waves. It is also noticeable that such observations were only made for class M_s 8 earthquakes.

5.2. Geomagnetic Field Effect

[44] We represent the ionospheric coupling factor α defined by relation (4) in Figure 13, using a radial wave vector **k** with 10° zenith angle. The ionospheric coupling factor map for the Wenchuan earthquake shows that the ionospheric coupled wave is less attenuated southward (α about 0.6) than northward (α about 0.35). This illustrates the southeastward directivity and the lack of signal in the north at near field noticed by *Afraimovich et al.* [2010]. At far field, in the sounded area (East China Sea) the ionospheric coupling factor variation is low. Consequently, the observed anisotropy is more related to the Rayleigh wave radiation pattern than to the geomagnetic field effect.

[45] At higher latitude in the Tokachi-Oki region, the geomagnetic field has a larger inclination angle of about 55°. Then, the ionospheric coupling factor is about 0.9 southward and 0.7 northward. This is also contributing to the northern attenuation observed on the TEC pattern observed with satellite 24 [*Heki and Ping*, 2005]. For satellite 13, the

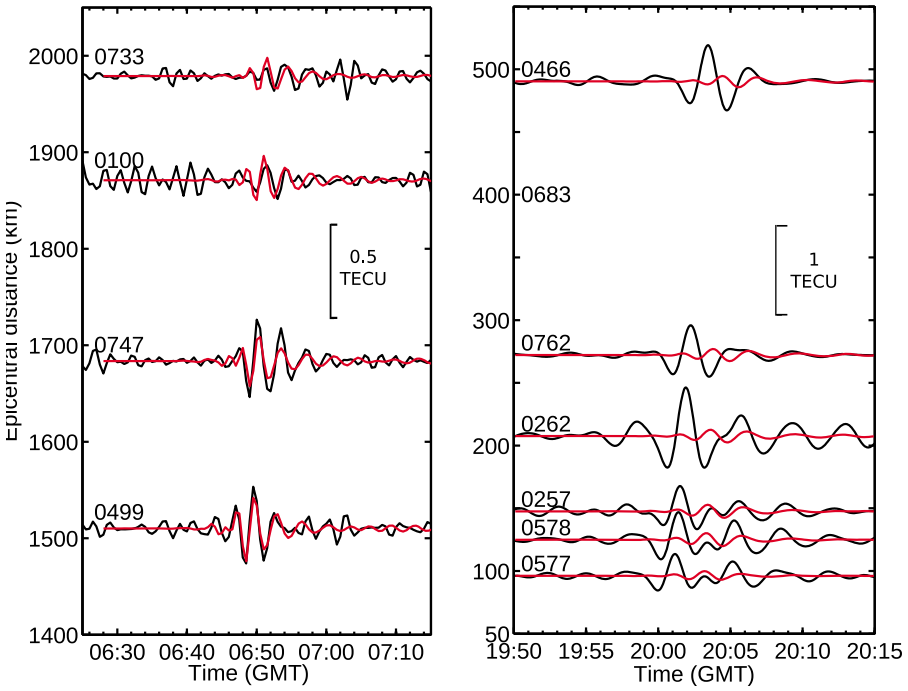

Figure 15. Observed (black) and modeled (red) STEC time series filtered between 4 and 10 mHz as function of the epicentral distance measured at the synthetics maximum. (a) At far field of the Wenchuan earthquake. The selected IPPs tracks are depicted on Figure 3. (b) At near field of the Tokachi-Oki earthquake. The IPPs tracks are depicted on Figure 5.

observation geometry is discussed in the following paragraph and will appear to be the largest contributing factor.

5.3. The Integration Step

[46] This final step allows us to compare our modeling with the data. The best agreement between our modeling and the data correlation amplitude and arrival time is found when we integrate the ionospheric local anomalies up to 360 km, for both cases: the Wenchuan and Tokachi-Oki events. This validates in an ad hoc way our viscous attenuation model up to 360 km height. A complete modeling must integrate other attenuation factors than viscosity, such as thermoconduction and also advection terms, which are not taken into account here and prevent it from using our viscosity model as real viscosity of the atmosphere.

[47] We first illustrate the observational biases on TEC caused by integration of the electron perturbation. These effects were predicted by *Georges and Hooke* [1970]. The electron perturbation is coherently summed when the line of sight is parallel to the perturbation wavefront and is canceled out when the line of sight is perpendicular. In other words, transionospheric techniques sound efficiently electron perturbations generated by atmospheric waves whose propagation vector **k** is perpendicular to the observation vector **s**, that is the direction vector of the line of sight [*Afraimovich et al.*, 2001].

[48] For the Wenchuan case, the observation geometry of satellite 14 is given in Figure 10. It generates a constructive integration of the electron density perturbation. As all the observation and wave vectors **s** and **k** have a relatively comparable geometry, the Rayleigh wave radiation pattern is almost unaffected. The resulting TEC patterns and waveforms shown in Figures 14 and 15 are in fairly good agreement with the observations.

[49] For the Tokachi-Oki case, satellites 24 and 13 respective geometry are shown in Figure 11. The destructive summation along satellite 24 line of sight explains why no Rayleigh speed waves are observed with the quasi-vertical satellite 24. The interpretation of the Rayleigh wave induced ionospheric pattern observed at near-field with satellite 13 is more complex. This observation geometry (about 50° of azimuth and 30° of elevation) enhances the Rayleigh wave induced ionospheric pattern in the west by phase integration while it attenuates it in the east by phase cancelation.

[50] It appears from the three steps of our modeling that the north-south anisotropy is related to the combination of three factors: the seismic source, the geomagnetic field and the observation geometry. They cause a strong attenuation of the Rayleigh wave coupled waves in the northeast and southeast quadrants, while the signal in the southwest quadrant keeps the source signature. There, the computed patterns in Figure 16 reconstruct fairly well the shape of the observed TEC images. However, the signal is still dominated at far field by the acoustically resonant N-shaped pulse. As a matter of fact, we show on the modeled traveltime diagrams that the oscillatory "R" (for Rayleigh) wave highlighted in Figure 4c can be modeled using our method and the used seismic source model. The waveforms comparison in Figure 1 also shows more precisely that only a small part of the perturbation is modeled. We also note in our synthetics maps a phase inversion, like on the data, which confirms its relation to the source.

[51] Several hypotheses in our models are far from being fully realistic, such as the point source approximation and a

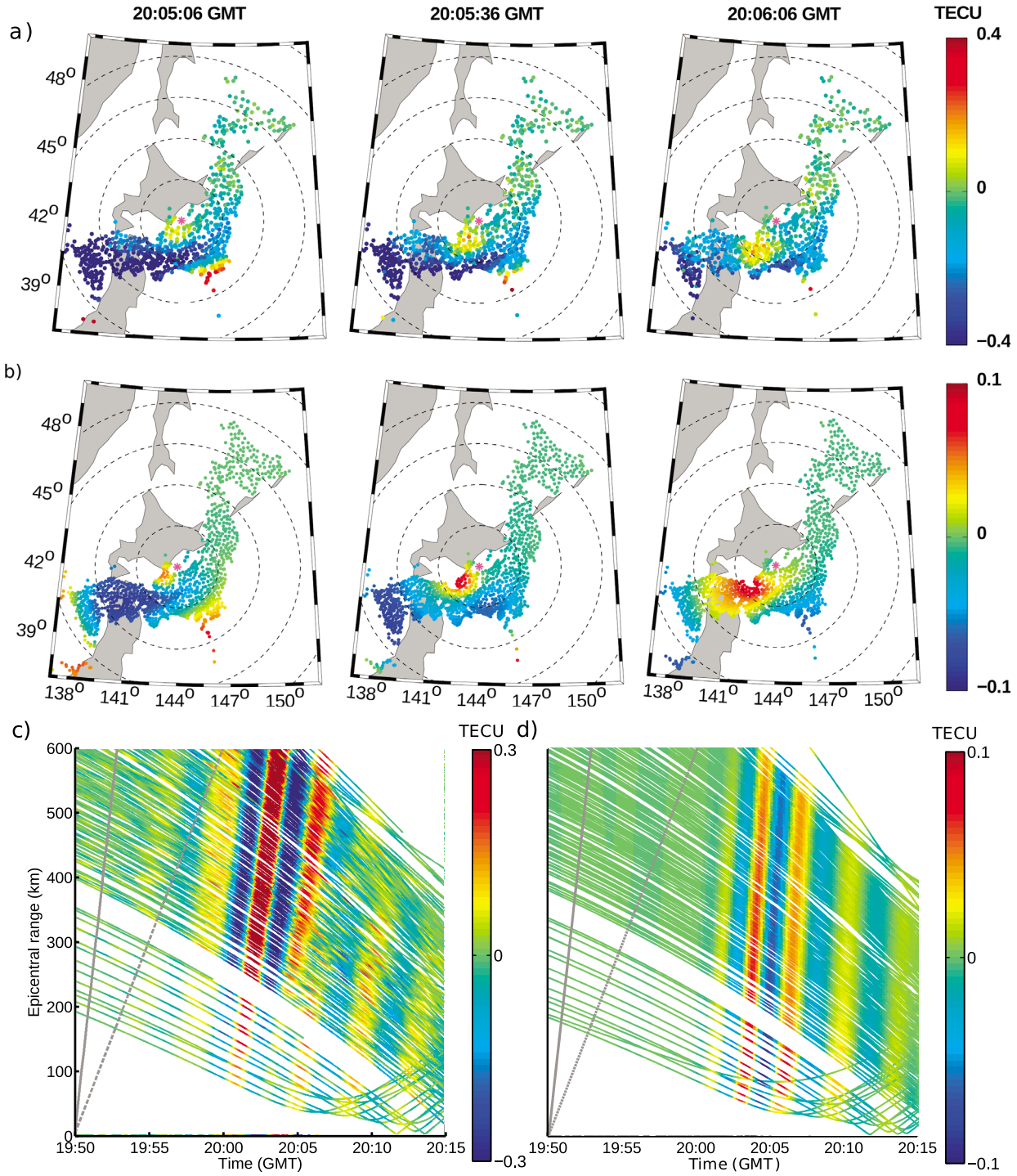

Figure 16. Same as Figure 14 but for the Tokachi-Oki earthquake. Only the eastern IPP tracks are depicted on the traveltime diagrams.

spherically symmetric standard Earth model, which might affect the ground vertical displacement, including the deficit of long-period signals described above on some stations. This first modeling does not incorporate the acoustic generated waves. Future works will focus on the modeling of the sharp primary pattern, the "N" wave highlighted by *Afraimovich et al.* [2001].

[52] Colocated measurements by Doppler sounder and GPS TEC techniques could also be of great interest to constrain the propagation and coupling mechanisms of Rayleigh wave induced ionospheric waves.

6. Conclusion

[53] We demonstrated the presence of Rayleigh wave induced ionospheric waves in the emission lobe of the Rayleigh wave radiation pattern of the 2008 Wenchuan earthquake and also above the offshore seismic source after

the 2003 Tokachi-Oki earthquake. We highlight from observations (see Table 3) that an elevation angle lower than 40° is a favorable geometrical condition for a satellite to sound Rayleigh wave induced ionospheric waves efficiently. In addition, ionospheric sounding points located in the direction of an emission lobe of the Rayleigh wave radiation diagram are the most sensitive to the passage of Rayleigh surface waves.

[54] By normal modes modeling and ionospheric coupling, we explain part of the observed pattern to the Rayleigh wave radiation pattern excited by both earthquakes. At far field, the good agreement between model results and observation in waveform, arrival time and patterns validates our model up to 360 km height. At near field, we were able to decipher the seismic source contribution from the ionospheric and observation geometry contributions, in the four quadrants around the epicenter. The network density and its wide coverage enabled through imaging the estimation of the fault azimuth in the southwest, where the Rayleigh wave induced ionospheric pattern is the least corrupted by the transionospheric sounding technique. However, the 0.2 TECU peak-to-peak modeled perturbation is only a fraction of the observed perturbation, showing that the modeling process is more complex and has to be improved to make possible an inversion of seismic source parameters from the observed radiation pattern. This will be made possible under the condition of using high-rate GPS data. As most of the GPS stations do not systematically transmit and archive their 1 Hz data, even after large earthquakes, an archiving effort will be required in order to conserve these exciting data for future works.

[55] **Acknowledgments.** L.R. is supported by French space agency CNES and SME NOVELTIS. We thank F. Crespon, A. Kherani, R. Garcia, G. Occhipinti, P. Coïsson, E. Astafyeva, D. Allain, and the NOVELTIS staff for constructive discussions. We especially acknowledge P. Coïsson for support in manuscript preparation and M. Coïsson for polishing our English. We thank K. Heki, Hokkaido University, Japan, and an anonymous referee for their constructive reviews. We also acknowledge the GSI and M. Murakami for providing us with 1 Hz GPS data of the GEONET Japanese GPS network. This work was supported by CNES with partial additional support of ONR (contract IONONAMI-N07-25). This is IPGP contribution 3144.

[56] Robert Lysak thanks Kosuke Heki and another reviewer for their assistance in evaluating this paper.

References

Afraimovich, E. L., N. P. Perevalova, A. V. Plotnikov, and A. M. Uralov (2001), The shock-acoustic waves generated by earthquakes, *Ann. Geophys.*, *19*, 395–409, doi:10.5194/angeo-19-395-2001.

Afraimovich, E. L., D. Feng, V. V. Kiryushkin, E. I. Astafyeva, S. Jin, and V. A. Sankov (2010), TEC response to the 2008 Wenchuan earthquake in comparison with other strong earthquakes, *Int. J. Remote Sens.*, *31*, 3601–3613, doi:10.1080/01431161003727747.

Aoi, S., R. Honda, N. Morikawa, H. Sekiguchi, H. Suzuki, Y. Hayakawa, T. Kunugi, and H. Fujiwara (2008), Three-dimensional finite difference simulation of long-period ground motions for the 2003 Tokachi-Oki, Japan, earthquake, *J. Geophys. Res.*, *113*, B07302, doi:10.1029/2007JB005452.

Artru, J., P. Lognonné, and E. Blanc (2001), Normal modes modelling of post-seismic ionospheric oscillations, *Geophys. Res. Lett.*, *28*(4), 697–700, doi:10.1029/2000GL000085.

Artru, J., T. Farges, and P. Lognonné (2004), Acoustic waves generated from seismic surface waves: propagation properties determined from Doppler sounding observations and normal-mode modelling, *Geophys. J. Int.*, *158*, 1067–1077, doi:10.1111/j.1365-246X.2004.02377.x.

Artru, J., V. Dučić, H. Kanamori, P. Lognonné, and M. Murakami (2005), Ionospheric detection of gravity waves induced by tsunamis, *Geophys. J. Int.*, *160*, 840–848, doi:10.1111/j.1365-246X.2005.02552.x.

Astafyeva, E., and K. Heki (2009), Dependence of waveform of near-field coseismic ionospheric disturbances on focal mechanisms, *Earth Planets Space*, *61*, 939–943.

Astafyeva, E., K. Heki, V. Kiryushkin, E. Afraimovich, and S. Shalimov (2009), Two-mode long-distance propagation of coseismic ionosphere disturbances, *J. Geophys. Res.*, *114*, A10307, doi:10.1029/2008JA013853.

Bilitza, D., and B. Reinisch (2008), International reference ionosphere 2007: Improvements and new parameters, *Adv. Space Res.*, *42*(4), 599–609, doi:10.1016/j.asr.2007.07.048.

Calais, E., and J. B. Minster (1995), GPS detection of ionospheric perturbations following the January 17, 1994, Northridge earthquake, *Geophys. Res. Lett.*, *22*, 1045–1048, doi:10.1029/95GL00168.

Calais, E., J. B. Minster, M. Hofton, and M. Hedlin (1998), Ionospheric signature of surface mine blasts from Global Positioning System measurements, *Geophys. J. Int.*, *132*, 191–202, doi:10.1046/j.1365-246x.1998.00438.x.

Clévédé, E., and P. Lognonné (2003), Higher order perturbation theory: 3D synthetic seismogram package, in *International Handbook of Earthquake and Engineering Seismology*, *Int. Geophys. Ser.*, vol. 81, Part 2, edited by P. C. J. William H.K. Lee, H. Kanamori and C. Kisslinger, pp. 1639–1639, Academic, Amsterdam, doi:10.1016/S0074-6142(03)80295-4.

Crespon, F. (2007), Tomographie 2d et 3d de l'ionosphère par GPS: Applications aux aléas géophysiques, Ph.D. thesis, Inst. de Phys. du Globe de Paris, Paris.

Dautermann, T. E., E. Calais, P. Lognonné, and G. Mattioli (2009), Lithosphere-Atmosphere-Ionosphere Coupling after the 2003 Explosive eruption of the Soufriere Hills Volcano, Montserrat, *Geophys. J. Int.*, *179*(3), 1537–1546, doi:10.1111/j.1365-246X.2009.04390.x.

Dučić, V., J. Artru, and P. Lognonné (2003), Ionospheric remote sensing of the Denali Earthquake Rayleigh surface waves, *Geophys. Res. Lett.*, *30*(18), 1951, doi:10.1029/2003GL017812.

Dziewonski, A. M., and D. L. Anderson (1981), Preliminary reference Earth model, *Phys. Earth Planet. Inter.*, *25*, 297–356, doi:10.1016/0031-9201(81)90046-7.

Georges, T. M., and W. H. Hooke (1970), Wave-induced fluctuations in ionospheric electron content: A model indicating some observational biases, *J. Geophys. Res.*, *75*, 6295–6308, doi:10.1029/JA075i031p06295.

Heki, K., and J. Ping (2005), Directivity and apparent velocity of the coseismic ionospheric disturbances observed with a dense GPS array, *Earth Planet. Sci. Lett.*, *236*, 845–855, doi:10.1016/j.epsl.2005.06.010.

Heki, K., Y. Otsuka, N. Choosakul, N. Hemmakorn, T. Komolmis, and T. Maruyama (2006), Detection of ruptures of Andaman fault segments in the 2004 great Sumatra earthquake with coseismic ionospheric disturbances, *J. Geophys. Res.*, *111*, B09313, doi:10.1029/2005JB004202.

Hickey, M. P., G. Schubert, and R. L. Walterscheid (2009), Propagation of tsunami-driven gravity waves into the thermosphere and ionosphere, *J. Geophys. Res.*, *114*, A08304, doi:10.1029/2009JA014105.

Hickey, M. P., G. Schubert, and R. L. Walterscheid (2010), Atmospheric airglow fluctuations due to a tsunami-driven gravity wave disturbance, *J. Geophys. Res.*, *115*, A06308, doi:10.1029/2009JA014977.

Hooke, W. (1970), Ionospheric response to internal gravity waves: 1. The F2 region response, *J. Geophys. Res.*, *75*, 5535–5544, doi:10.1029/JA075i028p05535.

Huba, J. D., G. Joyce, and J. A. Fedder (2000), Sami2 is Another Model of the Ionosphere (SAMI2): A new low-latitude ionosphere model, *J. Geophys. Res.*, *105*, 23,035–23,054, doi:10.1029/2000JA000035.

Kherani, E. A., P. Lognonné, N. Kamath, F. Crespon, and R. Garcia (2009), Response of the ionosphere to the seismic triggered acoustic waves: Electron density and electromagnetic fluctuations, *Geophys. J. Int.*, *176*, 1–13, doi:10.1111/j.1365-246X.2008.03818.x.

Kobayashi, N. (2007), A new method to calculate normal modes, *Geophys. J. Int.*, *168*, 315–331, doi:10.1111/j.1365-246X.2006.03220.x.

Lognonné, P. (1991), Normal modes and seismograms in an anelastic rotating Earth, *J. Geophys. Res.*, *96*, 20,309–20,319, doi:10.1029/91JB00420.

Lognonné, P. (2009), Seismic waves from atmospheric sources and Atmospheric/Ionospheric signatures of seismic waves, in *Infrasound Monitoring for Atmospheric Studies*, edited by A. Le Pichon, E. Blanc, and A. Hauchecorne, pp. 281–304, Springer, Dordrecht, Netherlands.

Lognonné, P., E. Clévédé, and H. Kanamori (1998), Computation of seismograms and atmospheric oscillations by normal-mode summation for a spherical Earth model with realistic atmosphere, *Geophys. J. Int.*, *135*, 388–406, doi:10.1046/j.1365-246X.1998.00665.x.

Lognonné, P., J. Artru, R. Garcia, F. Crespon, V. Ducic, E. Jeansou, G. Occhipinti, J. Helbert, G. Moreaux, and P. Godet (2006), Ground-

based GPS imaging of ionospheric post-seismic signal, *Planet. Space Sci.*, *54*, 528–540, doi:10.1016/j.pss.2005.10.021.

Mannucci, A. J., B. D. Wilson, D. N. Yuan, C. H. Ho, U. J. Lindqwister, and T. F. Runge (1998), A global mapping technique for GPS-derived ionospheric electron content measurements, *Radio Sci.*, *33*, 565–582, doi:10.1029/97RS02707.

Maus, S., et al. (2005), The 10th generation international geomagnetic reference field, *Phys. Earth Planet. Inter.*, *151*, 320–322, doi:10.1016/j.pepi.2005.03.006.

McLeod, M. A. (1966), Sporadic E theory. I. Collision-geomagnetic equilibrium, *J. Atmos. Sci.*, *23*, 96–109, doi:10.1175/1520-0469(1966)023<0096:SETICG>2.0.CO;2.

Occhipinti, G. (2006), Observations multi-paramètres et modélisation de la signature ionosphérique du grand séisme de sumatra, Ph.D. thesis, Inst. de Phys. du Globe de Paris, Paris.

Occhipinti, G., P. Lognonné, E. A. Kherani, and H. Hébert (2006), Three-dimensional waveform modeling of ionospheric signature induced by the 2004 Sumatra tsunami, *Geophys. Res. Lett.*, *33*, L20104, doi:10.1029/2006GL026865.

Occhipinti, G., E. A. Kherani, and P. Lognonné (2008), Geomagnetic dependence of ionospheric disturbances induced by tsunamigenic internal gravity waves, *Geophys. J. Int.*, *173*, 753–765, doi:10.1111/j.1365-246X.2008.03760.x.

Occhipinti, G., P. Dorey, T. Farges, and P. Lognonné (2010), Nostradamus: The radar that wanted to be a seismometer, *Geophys. Res. Lett.*, *37*, L18104, doi:10.1029/2010GL044009.

Picone, J., A. Hedin, D. Drob, and A. Aikin (2002), NRLMSISE-00 empirical model of the atmosphere: Statistical comparisons and scientific issues, *J. Geophys. Res.*, *107*(A12), 1468, doi:10.1029/2002JA009430.

Rolland, L. M., G. Occhipinti, P. Lognonné, and A. Loevenbruck (2010), Ionospheric gravity waves detected offshore Hawaii after tsunamis, *Geophys. Res. Lett.*, *37*, L17101, doi:10.1029/2010GL044479.

Sagiya, T. (2004), A decade of GEONET: 1994–2003 The continuous GPS observation in Japan and its impact on earthquake studies, *Earth Planets Space*, *56*, 29–41.

Watada, S., and H. Kanamori (2010), Acoustic resonant oscillations between the atmosphere and the solid Earth during the 1991 Mt. Pinatubo eruption, *J. Geophys. Res.*, *115*, B12319, doi:10.1029/2010JB007747.

Watada, S., T. Kunugi, K. Hirata, H. Sugioka, K. Nishida, S. Sekiguchi, J. Oikawa, Y. Tsuji, and H. Kanamori (2006), Atmospheric pressure change associated with the 2003 Tokachi-Oki earthquake, *Geophys. Res. Lett.*, *33*, L24306, doi:10.1029/2006GL027967.

Woodhouse, J. H. (1988), The calculation of eigenfrequencies and eigenfunctions of the free oscillations of the Earth and the Sun, in *Seismological Algorithms*, edited by D. Dornboos, pp. 321–370, Academic, New York.

Yagi, Y. (2004), Source rupture process of the 2003 Tokachi-Oki earthquake determined by joint inversion of teleseismic body wave and strong ground motion data, *Earth Planets Space*, *56*, 311–316.

P. Lognonné and L. M. Rolland, Géophysique Spatiale et Planétaire, Institut de Physique du Globe de Paris, Sorbonne Paris Cité, Univ. Paris Diderot, UMR 7154 CNRS, 4 Av. de Neptune, F-94100 Saint-Maur des Fossés, France. (rolland@ipgp.fr)

H. Munekane, Geospatial Information Authority of Japan, Geography and Crustal Dynamics Research Center, Kitasato-1, Tsukuba, 305-0811, Japan.